Spectroscopic properties of newly flux grown and highly Yb3+-doped cubic RE2O3 (RE=Y, Gd, Lu) laser crystals

Matias Velázquez, Philippe Veber, Gabriel Buşe, Yannick Petit, Philippe Goldner, Veronique Jubera, Daniel Rytz, Anaël Jaffres, Mark Peltz, Volker Wesemann, et al.

Spectroscopic properties of newly flux grown and highly Yb^{3+}-doped cubic RE_2O_3 (RE = Y, Gd, Lu) laser crystals

Matias Velázquez*[a], Philippe Veber[a], Gabriel Buşe[a], Yannick Petit[a], Philippe Goldner[b], Véronique Jubera[a], Daniel Rytz[c], Anaël Jaffres[b], Mark Peltz[c], Volker Wesemann[c], Patrick Aschehough[b], Gérard Aka[b]

[a] CNRS, Université de Bordeaux, ICMCB, UPR 9048, 87 avenue du Dr. A. Schweitzer, 33608 Pessac cedex, France
[b] PSL Research University, Chimie ParisTech – CNRS, Institut de Recherche de Chimie Paris, 75005 Paris, France
[c] Fee-GmbH, Struthstrasse 2, 55743 Idar-Oberstein, Germany

Abstract : We have developed laser grade and highly Yb^{3+}-doped cubic rare-earth sesquioxides (RE_2O_3, RE = Y, Gd, Lu) single crystals by means of a newly designed high-temperature solution growth method which gives them spectroscopic properties different from those obtained by high-temperature solidification methods. Absorption and emission cross sections, visible anti-Stokes emission, fluorescence decays of the new cubic $Gd_2O_3:Yb^{3+}$ single crystals are presented and compared to those of $Y_2O_3:Yb^{3+}$ and $Lu_2O_3:Yb^{3+}$ crystals. The case of cubic $Gd_2O_3:Yb^{3+}$ is particularly interesting since its basic spectroscopic properties have never been detailed and we were capable of achieving Yb-doping level as high as 20%.

1. Introduction

Since at least 20 years, the growth and development of laser grade cubic RE_2O_3 (RE=Y,Gd,Lu,Sc) single crystals have been proceeding apace [1-5]. In 2010, a successful power scaling of a single passively mode-locked thin-disk laser cavity was achieved with $Lu_2O_3:Yb^{3+}$ crystals which delivered an average power of 141 W under diode pumping at 976 nm [4]. In 2011, it is an impressive 670 W output power that was obtained in CW regime also using thin disk technology with a $Lu_2O_3:Yb^{3+}$ crystal [6]. Several methods have again been put forward these last three years to grow pure and RE'^{3+}-doped (RE'=Tm, Er or Yb) cubic RE_2O_3 (RE=Y, Lu or Sc) single crystals [2,5,7,8]. In this work, we present spectroscopic characterizations of newly flux grown cubic and Yb^{3+}-doped RE_2O_3 (RE=Y,Gd,Lu) single crystals [5], focusing more particularly on $Lu_2O_3:Yb^{3+}$ and $Y_2O_3:Yb^{3+}$ crystals, while also showing the heretofore unknown absorption, stimulated emission and anti-Stokes emission spectra of highly-doped cubic $Gd_2O_3:Yb^{3+}$ crystals. Our flux growth technique validated with $Y_2O_3:Yb^{3+}$ and $Gd_2O_3:Yb^{3+}$ crystals laser operation, which exhibited laser efficiencies comparable to those of crystals obtained by means of other growth techniques [9]. We emphasize that this flux growth process, which uses $Li_6RE(BO_3)_3$ (RE=Y, Gd, Lu) as the solvent working at half the melting temperature of the corresponding RE_2O_3, allows to achieve optimal doping for high-power laser applications, impedes the dissolution of OH^- groups in the crystals, avoids the reduction of Yb^{3+} ions into Yb^{2+} ones (and its resulting absorption lines around 600, 520 and 480 nm [10]), favours broader absorption and emission lines. Such a broadness, as well as anti-Stokes emission spectra, are discussed within the scope of an exhaustive chemical analysis of $Lu_2O_3:Yb^{3+}$ and $Gd_2O_3:Yb^{3+}$ crystals by GDMS. Moreover, it is found that in $Y_2O_3:Yb^{3+}$ crystals, up to an Y^{3+} substitution rate for Yb^{3+} cations of 6.5 %, this growth technique drastically hinders the formation kinetics of Yb^{3+} pairs that would lead to a cooperative emission around 500 nm [10,11] detrimental to the fluorescence quantum yield of the Yb^{3+} ions near infrared (NIR) emission.The intermetallic $SmCo_5$ was prepared by melting of stoichiometric amounts of the constituent elements under a purified argon atmosphere in an induction levitation furnace. The purity of the starting materials was as follows: Sm, 99.9%; Co, 99.99%. Before milling, the powder was sieved at 100 µm in a dry-box. $SmCo_5$ particles were obtained by grinding using a Fritsch P5 high-energy apparatus. The ratio weight of ball over weight of sample is 15 and the rotation speed was fixed at 300 rpm. The diameter of the ball used for grinding is 10 mm. The applied pressure of H_2 was 1.1 MPa.

2. Experimental

All the experimental details about the growth and characterization of the samples have been given elsewhere [5,12]. The Yb^{3+} contents were determined by EPMA/WDS over large facets and the following average compositions in the crystals that were studied in this work are: $Lu_{1.91}Yb_{0.09}O_3$, $Lu_{1.86}Yb_{0.14}O_3$, $Y_{1.87}Yb_{0.13}O_3$ and $Gd_{1.72}Yb_{0.28}O_3$. So far, the highest concentrations that we could achieve are $Lu_{1.86}Yb_{0.14}O_3$, $Y_{1.69}Yb_{0.31}O_3$ and $Gd_{1.61}Yb_{0.39}O_3$, and we have not identified the solubility limit. The ratio of final Yb^{3+} concentration in the crystals over initial Yb^{3+} concentration in the growth melt was determined to be ≈2.1 in Gd_2O_3, ≈1.6 in Y_2O_3 and ≈0.9 in Lu_2O_3. Magnetic susceptibility was measured in field-cooled

mode using a Quantum Design SQUID MPMS XL magnetometer operated in the 4.2−354 K temperature range under an applied magnetic field of 5 mT. A high-temperature HEM-grown $Lu_{1.965}Yb_{0.035}O_3$ crystal from Fee GmbH, of mass 185.7 mg, and a flux-grown $Lu_{1.86}Yb_{0.14}O_3$ crystal of mass 199.7 mg were mounted in a capsule placed in a straw. The negligibly small diamagnetic contribution of the capsule was not subtracted from our data. Visible and NIR absorption spectra were recorded with a Varian Cary 5000 spectrophotometer. Continuous-wave emission spectra were collected at room temperature in the visible and NIR spectral range by exciting the sample between 910 and 954 nm, and recorded with a HORIBA Jobin Yvon spectrometer. Exhaustive trace element chemical analysis (75 elements except C, H, O, N) was performed by GDMS on a single crystal of composition $Lu_{1.91}Yb_{0.09}O_3$, and another single crystal of composition $Gd_{1.72}Yb_{0.28}O_3$.

3. Experimental

3.1 Absorption and emission spectra, Yb^{3+} ions radiative lifetimes

The absorption and reciprocity method (RM)-calibrated emission spectra of $Lu_{1.91}Yb_{0.09}O_3$ and $Y_{1.87}Yb_{0.13}O_3$ single crystals have been shown and interpreted elsewhere [5,12]. Yb^{3+}-doped Gd_2O_3 absorption spectrum is shown in Fig. 1. Calibration in cross-section units was performed with a concentration of 3.6 10^{21} cm^{-3}, that is, 14 % of Yb^{3+} cations substituted for Gd^{3+} ones. Such a concentration is certainly much higher than the concentration that would optimize the experimental lifetime. This optimum, resulting from the antagonistic effects of self-trapping and concentration quenching, was found to be 1.6 10^{20} cm^{-3} in Y_2O_3:Yb^{3+} crystals [13]. The high substitution rate achieved in our crystals should permit to reduce its thickness down to a few hundred microns, allowing for an efficient cooling while maintaining a high absorption yield under thin-disk laser operation. The fact that the 5-4 transition peaks at 1074 nm proves the cubic structure of the crystals, in which ¾ of the Gd^{3+} cations exhibit a C_2 point group symmetry and ¼ of them a C_{3i} point group one. Indeed, in monoclinic Gd_2O_3 crystals, this transition is shifted at ~1105 nm [14]. The inset in figure 1 shows an energy level diagram and the transition lines actually observed are compatible with the expected crystal-field Yb^{3+}-ion manifold splitting for the C_2-point symmetry. The forced electric dipole contribution to this transition oscillator strength is much higher (f^{fED}/f^{MD}~11) in Gd_2O_3 than in Y_2O_3 and Lu_2O_3 crystals [5]. The radiative lifetime calculated with this absorption spectra, taking a degeneracy ratio of the $^2F_{5/2}$ and $^2F_{7/2}$ multiplets $g(^2F_{5/2})/g(^2F_{7/2})$=¾ and an average wavelength ~950.8 nm, is about 0.495 ms. Such a small value must be corrected by means of Auzel's method [15]. Indeed, by calculating the oscillator strength and the spontaneous emission probability with, in his notations [15], α=1.67 10^{-20} cm^2, β=1.417 10^{-20} cm^2, γ=0.183 10^{-20} cm^2, $\delta\approx0$ cm^2, and the energy level diagram given in figure 1's inset to estimate each multiplet's partition function, we find $g(^2F_{5/2})/g(^2F_{7/2})\approx1.49$, hence a radiative lifetime ≈0.982 ms, slightly lower than the radiative lifetime estimated for Y_2O_3:Yb^{3+} crystals (1.1 ms, [5,11,12]). The Yb^{3+}-doped Gd_2O_3 emission spectrum shown in Fig. 1 was calibrated in cross-section units by the method discussed by Payne *et al.* [16]. The radiative lifetime necessary to match the Fuchtbauer-Ladenburg (FL)-transformed spectrum with the reciprocity method (RM)-transformed one is ~67 % higher than the correct radiative lifetime determined above. The origin for such a discrepancy is likely to be due to a strong reabsorption effect, which was confirmed by varying the excitation wavelength at 910, 932 and 954 nm. The 5→3 emission line profiles in our crystals are different from those of Hraïech PhD thesis work [11], in the sense that they are broader (FWHM≈15.6 *vs* 13.7 nm in Y_2O_3:Yb^{3+} and FWHM≈15.1 *vs* 12.4 nm in Lu_2O_3:Yb^{3+} crystals [5,11,12]) and that we do not observe any covalence effect on the cross-section peak value in Lu_2O_3 with respect to Y_2O_3 crystals.

The 5→4 emission line cross-section peak values also are much smaller and the FWHM higher in our samples than in hers [11]. Moreover, the 5→3 emission peak cross section is ~25% higher in $Gd_{1.72}Yb_{0.28}O_3$ crystals than in $Y_{1.87}Yb_{0.13}O_3$ and $Lu_{1.91}Yb_{0.09}O_3$ counterparts [5], which is likely to be due to some covalent effect. The transmission spectra measured in the range 200-800 nm (Fig. 2) also establish the absence of absorption lines due to Yb^{2+} ions, likely to appear around 600, 520 and 480 nm [10]. FTIR spectra (Fig. 2) were devoid of any absorption line around 3 μm in Lu_2O_3:Yb^{3+} crystals, and a small one was detected in Y_2O_3:Yb^{3+} crystals which, once adequately corrected for Mie, Rayleigh and Urbach diffractions and integrated, leads to an OH^- concentration [5,11,12] of ≈2.2 10^{21} cm^{-3}. Indeed, for the 0-3.4 10^{21} cm^{-3} OH^--concentration range in Y_2O_3:Yb^{3+} crystals, one can extract an approximate law from Hraïech PhD thesis work [11], $n_{OH^-}(cm^{-3})\approx6.9348\ 10^{19}$ $A(cm^{-2})$, with A being the area below the absorption coefficient (cm^{-1}) (versus wavenumbers (cm^{-1})) peak assigned to the OH^- groups absorption. In order to check the presence of Yb^{3+} in Lu_2O_3 crystals, as well as that of possible other TM^{3+} contaminants (TM=transition metal), we measured the magnetic susceptibility, expressed in the MKSA units system, of two single crystals, one $Lu_{1.86}Yb_{0.14}O_3$ flux-grown crystal and one HEM-grown $Lu_{1.965}Yb_{0.035}O_3$ crystal from Fee GmbH (figure 3).

The $Lu_{1.86}Yb_{0.14}O_3$ flux-grown crystal exhibit a Curie-Weiss behavior from ~110 K to at least 354 K, with a Curie constant C≈0.097 K and a paramagnetic Curie temperature θ_p≈-43.1 K, showing that the overall magnetic couplings are antiferromagnetic, and leading to an effective magnetic moment μ_{eff}≈4.29 μ_B/Yb^{3+}. This value corresponds to 94.7% of the theoretical free ion value. The discrepancy only slightly exceeds the error bar (~5%) and is likely to be due to the ionocovalent nature of the chemical bond. In the HEM-grown $Lu_{1.965}Yb_{0.035}O_3$ crystal, it is not possible to identify a temperature range broad enough to perform a Curie-Weiss fit. Instead of this, it looks like there are three successive linear segments of the inverse susceptibility over the same temperature range (from ~110 K to 354 K), which suggests that Yb^{3+} cations are distributed over several crystallographic sites which do not appear in the flux-grown crystal. In addition, it is obvious that the Curie constant is weaker, which taking into account the weaker Yb concentration, suggests that their magnetic moment is higher than both the effective Yb^{3+} magnetic moment determined above and the theoretical free ion value. As Yb^{2+} cations are isoelectronic with Lu^{3+} ones, they have no magnetic moment and display a weak diamagnetic response to the magnetic field. Consequently, we are led to assume that this "multi Curie-Weiss" behavior might be due to the dissolution of paramagnetic impurities, such as Fe^{3+} ($\mu_{free\text{-}ion}$≈5.95 μ_B/Fe^{3+}), Tm^{3+} ($\mu_{free\text{-}ion}$≈7.56 μ_B/Tm^{3+}), Gd^{3+} ($\mu_{free\text{-}ion}$≈7.94 μ_B/Gd^{3+}) or Er^{3+} ($\mu_{free\text{-}ion}$≈9.58 μ_B/Er^{3+}).

3.2 Yb^{3+}-ions fluorescence decays and NIR fluorescence quantum yield

Yb^{3+}-ions fluorescence decays under resonant excitation are exponential over three times the experimental lifetime (Fig. 4), which is 0.93 ms for Y_2O_3:Yb^{3+} and 1.02 ms for Lu_2O_3:Yb^{3+} single crystals. The former value, when inserted in the τ_{exp} *versus* [Yb^{3+}] curve of Auzel [13], leads to an Yb^{3+}-concentration value consistent with the Yb^{3+} ions concentrations characterized by both X-ray diffraction and electron probe microanalysis [5], and turns out to be slightly lower than the highest values (~1 ms) found in the literature [10,11]. The latter value stands among the highest ones ever obtained in this family of crystals, suggesting that Lu_2O_3:Yb^{3+} single crystals are optimally doped [10,13]. The $\sigma_{em}\tau_{exp}$ storage parameter around 1030 nm is on the order of magnitude of 7 10^{-24} cm^2.s, that is, one order of magnitude lower than that of state-of-the-art YAG:Nd^{3+} crystals at 1064 nm, but still likely to make these crystals competitive for energy storage with a view to high average or peak output powers delivery in diode-pumped laser operation. The exponential fit is less convincing for the Gd_2O_3:Yb^{3+} crystal but however leads to an experimental lifetime 0.48 ms, which is likely to be due to the high substitution rate. To explain the difference between the experimental and the radiative lifetimes, which leads for example to a fluorescence quantum yield of ~85 % in the Y_2O_3:Yb^{3+} crystals, one must consider a series of mechanisms competing with the radiative one [11,17]. The non radiative multiphonon emission relaxation mechanism can be looked upon as negligible. As a matter of fact, for Y_2O_3:Yb^{3+} crystals, several classical and refined gap laws have been established [18-21], and for ΔE=9704 cm^{-1} [5], the probability for this mechanism is, to the maximum, ~10^{-4} s^{-1}. Another mechanism which can be discarded is that of radiative quenching by excitation of OH^- vibrations. Indeed, for the OH^- concentration determined in our Y_2O_3:Yb^{3+} crystals, the decay time series of measurements as a function of proton content performed by Hraïech [11] allows for an estimate of this mechanism's probability ≈67 s^{-1}. For the 7.1 10^{20} - 3.4 10^{21} cm^{-3} OH^--concentration range in Y_2O_3:Yb^{3+} crystals, one can extract from her measurements an approximate law, $\tau_{OH\text{-}}$(s)≈-2.1749 10^{-24} $n_{OH\text{-}}$(cm^{-3}) + 0.0199353, with $\tau^{-1}_{OH\text{-}}$ the contribution of this mechanism to the total non radiative relaxation probability, assumed to be independent on the other contributions.

3.3 Anti-Stokes (AS) emission spectra, Er^{3+} and Tm^{3+} impurity ions fluorescence transients

Looking for relevant mechanisms, such as Yb^{3+} pairs cooperative luminescence [22] and Yb-RE energy transfers by upconversion (ETUs) [23-25] competing with the NIR radiative one [17], we carried out anti-Stokes emission spectroscopy on our crystals (Fig. 5). According to the purity assessment performed by means of mass spectroscopy by the raw powder suppliers for 5N Y_2O_3, 5N Gd_2O_3, 4N Lu_2O_3 and 4N or 3N8 Yb_2O_3 raw powders, the maximum impurity concentration that we should expect in the initial loads that we prepared for growth runs are gathered in table 1.

Figure 5 shows in the three crystals the typical AS emissions from Er^{3+} ($^4S_{3/2}$, $^4F_{9/2}$) and Tm^{3+} ($^1G_4$) ions in the visible range. At an excitation power of ~1 mW, no AS emission from the Er^{3+} $^2H_{9/2}$ multiplet around 410 nm was observed [11], suggesting a very low concentration of this ion. In the case of the Lu_2O_3:Yb^{3+} crystal a low Er concentration was indeed found by GDMS analysis. No Li nor B traces are found at the ppm level in Yb_2O_3, Gd_2O_3 and Y_2O_3 starting products and yet they were found in the final crystal in substantial amount (~3 10^{17} cm^{-3}), which firmly establishes their dissolution in atomic forms because their concentration ratio is not that expected from the flux composition. As these impurities were not found in Hraïech crystals [11], we believe they might constitute part of the explanation for the higher inhomogeneous broadening of the 5-3 and 5-4 emission lines observed in our crystal. Another contribution to the inhomogeneous broadening could lie in the elastic strain field arising from flux inclusions, especially in Y_2O_3:Yb^{3+} crystals where the

exhaustive GDMS chemical analysis was not possible. Table 1 suggests that our flux growth method has the ability to lower the Er, Tm, Nd, Dy and Fe contents of Lu_2O_3:Yb^{3+}. The inset in Fig. 5 displays a zoom of the data in the blue-green spectral range (500-525 nm) together with a convolution of the NIR spectrum by itself indicating the possible peaks likely to arise from cooperative luminescence from Yb^{3+} pairs (with characteristic lifetime $\tau_{exp}/2$). This mechanism usually gives emission lines in cubic Lu_2O_3:Yb^{3+} single crystals at 513 nm [10], 505 and 520 nm [11] and can be related to Yb^{3+} cluster formation [26,27]. The absence of such cooperative emission lines in our measurements, even at excitation powers higher than 1 mW, suggests that Yb^{3+}-ions pairs were not formed in the course of our crystal growth process. This might be a result of hindered formation kinetics due to the fact that the crystals grow at half their melting point temperature, at least for Yb^{3+} substitution for RE^{3+} cations rates up to 6 %. As a matter of fact, in the case of Gd_2O_3:Yb^{3+} crystals, the large substitution rate achieved in this study makes the Yb-pairs formation unavoidable and a very broad emission is observed between 495 and 520 nm, where cooperative emission lines are expected (502 and 517 nm).

Ln-Ln plots of the AS emission intensity *vs* excitation power, far from saturation, are shown in Fig. 6 to evidence the two- and three-photon processes involved in the population of the Er^{3+} $^4S_{3/2}$ and $^4F_{9/2}$ multiplets, and of the Tm^{3+} $^1G_4$ multiplet. As non radiative phonon emissions relaxations are also involved in these Yb-RE ETUs, there are some deviations from the expected 2 and 3 slopes. In the case of Tm^{3+} ions, the stronger deviation from the expected value may also arise from other transfer or emission mechanisms simultaneously at play under these excitation conditions.

Er^{3+} ($^4S_{3/2}$) and Tm^{3+} ($^1G_4$) fluorescence transients under non resonant excitation at 976 nm in $Lu_{1.91}Yb_{0.09}O_3$, $Y_{1.87}Yb_{0.13}O_3$ and $Gd_{1.72}Yb_{0.28}O_3$ crystals are shown in Fig. 7. They exhibit two main features: (i) an intensity rise with a finite characteristic time due to the multiple photon absorptions, intermediate non radiative decays and Er^{3+} $^4S_{3/2}$ and Tm^{3+} $^1G_4$ multiplets experimental lifetimes; (ii) once the intensity maximum is reached, a non exponential decay with a decay time related to the Yb^{3+} $^2F_{5/2}$ multiplet lifetime (typically $\tau_{exp}/2$). Since the rise time and the average decay times for both ions dissolved in these crystals are on the order of a few hundreds of µs, it is clear that under high excitation powers, or at high Er^{3+} and Tm^{3+} concentrations, such mechanisms are likely to deplete the Yb^{3+} $^2F_{5/2}$ multiplet and to increase the heat load released in the crystal. As a first approach, we could fit these transients with Buisson-Vial's kinetic model [28] and find that $W_{rise}\approx7967$ s^{-1} and $W_{dec}\approx1415$ s^{-1} for the Er^{3+} $^4S_{3/2}$ AS emission, and that $W_{rise}\approx2417$ s^{-1} and $W_{dec}\approx2406$ s^{-1} for the Tm^{3+} $^1G_4$ AS emission in lutetia crystals. In the case of Er^{3+} $^4S_{3/2}$ fluorescence transient, the higher intensity slope near t=0, as compared to that of Tm^{3+} $^1G_4$, may also mean that in the former ions a GSA+ESA sequence involving the Er^{3+} $^4I_{11/2}$ multiplet is efficient in feeding the $^2H_{11/2}$-$^4S_{3/2}$ levels, after a fast non radiative relaxation from the $^4F_{7/2}$ multiplet by multiphonon emission.

3.4 RE^{3+} impurities partition in the crystals

The rare earth (above all Er, Tm, Nd and Dy) contents in our flux grown crystals probably give the beginnings of an explanation for the trend in laser performances obtained recently [9]. With a pumping wavelength λ_P=977 nm, an absorption yield of $\eta_{abs}\approx98$ %, a pump beam diameter of ϕ_P=60 µm and an output coupler of T_{OC}=4 % in $Gd_{1.72}Yb_{0.28}O_3$ and of 6 % in $Y_{1.87}Yb_{0.13}O_3$, the following thresholds and laser slopes in quasi continuous regime were obtained:

- in $Gd_{1.72}Yb_{0.28}O_3$, P_{dp}=729 mW, η_{dp}=33 %, $P_{Ti:Sa}$=464 mW, $\eta_{Ti:Sa}$=45 %, and in continuous regime η_{dp}=26 % ("dp" means diode pump);

- in $Y_{1.87}Yb_{0.13}O_3$, P_{dp}=307 mW, η_{dp}=58 %, $P_{Ti:Sa}$=212 mW, $\eta_{Ti:Sa}$=66 %, and in continuous regime η_{dp}=51 %.

The main counterintuitive facts about our growth process are twofold: firstly, it permits to reach unprecedented substitution levels, secondly, it dissolves more Yb^{3+} cations in Gd_2O_3 than in Y_2O_3, and more Yb^{3+} cations in Y_2O_3 than in Lu_2O_3. Our growth experiments suggest that the solubility limit of Gd_2O_3 (main solute) in $Li_6Gd(BO_3)_3$ (solvent) is higher than that of Yb_2O_3 (secondary solute), and that the situation is reversed for Lu_2O_3 (main solute) in $Li_6Lu(BO_3)_3$ (solvent), in such proportions that compensate for solid state thermodynamics. As a matter of fact, in the TM impurity concentration range 10^{19} cm^{-3} and less, the $Li_6Gd(BO_3)_3$ solvent/Gd_2O_3 crystal partition equilibrium coefficient, k_0, reads:

$$k_0 \approx \frac{\gamma'^{LGB,sat}_{Gd_2O_3}}{\gamma'^{LGB,sat}_{TM_2O_3}} \frac{x^{LGB,sat}_{Gd_2O_3}}{x^{LGB,sat}_{TM_2O_3}} e^{\frac{\left[\Delta S^{s}_{\theta,TM}+\Delta S^{LGB}_{\theta,Gd}-\Delta S^{LGB}_{\theta,TM}\right]}{R}} e^{\frac{\left[\Delta H^{LGB}_{d,TM_2O_3}-\Delta H^{LGB}_{d,Gd_2O_3}-\Delta U_{lat}-8\pi G r_{Gd}\left(r_{TM}-r_{Gd}\right)^2\right]}{RT}}$$

provided that the entropy changes upon dissolution of any TM_2O_3 in solid Gd_2O_3 and in liquid $Li_6Gd(BO_3)_3$, and of Gd_2O_3 in liquid $Li_6Gd(BO_3)_3$, are mainly of vibrational origin. In this expression, $\gamma^{LTB,sat}$ and $x^{LTB,sat}$ stand for the activity coefficient and solubility limit of Gd_2O_3 or any TM_2O_3 in saturated liquid $Li_6Gd(BO_3)_3$. Since the first ratio is usually close to 1, the solubility

limits ratio appears as the most important term which is likely to compensate for the "solid state thermodynamics" terms playing a role in the exponentials brackets [29]. ΔS's and ΔH's are entropy and enthalpy changes upon dissolution of Gd_2O_3 in liquid $Li_6Gd(BO_3)_3$ or any TM_2O_3 in solid Gd_2O_3 or in liquid $Li_6Gd(BO_3)_3$. Dissolution enthalpy changes in high temperature melts are to be measured by drop calorimetry and cannot *a priori* be easily calculated. ΔU_{lat}, G and r symbolize the lattice energy change upon dissolution in the crystalline state between pure TM_2O_3 and pure Gd_2O_3, the Gd_2O_3 shear modulus and the ionic radii of Gd^{3+} and TM^{3+} cations in the relevant coordination number, respectively. Since any TM^{3+} solubility increases with native Schottky defects concentrations in solid Gd_2O_3 and in liquid $Li_6Gd(BO_3)_3$, and the same occurs for Gd^{3+} in liquid $Li_6Gd(BO_3)_3$, one understands that the lower the solubility limit of Gd_2O_3 in liquid $Li_6Gd(BO_3)_3$ with respect to that of any other TM_2O_3, the lower its contamination by any other TM will be. The ratio of Li over B concentrations (~0.9 in Lu_2O_3 and ~4.6 in Gd_2O_3) clearly discards the presence of solvent inclusions in the investigated samples but the effect of the solvent is evidenced. A logical consequence of this thermodynamic property of the $Li_6RE(BO_3)_3$ (RE=Lu,Gd,Y) solvent is that while $Li_6Lu(BO_3)_3$ purifies Lu_2O_3:Yb^{3+} crystals in Er^{3+}, Tm^{3+}, Nd^{3+}, Dy^{3+} and Fe^{3+} impurities, the $Li_6Gd(BO_3)_3$ solvent contaminates Gd_2O_3:Yb^{3+} with the same elements, thus explaining the anti-Stokes emission transients and part of the fluorescence quantum yield and closely related laser slopes.

4. Conclusions

We have shown that Yb^{3+}-doped cubic RE_2O_3 (RE=Y,Gd,Lu) single crystals grown by the widely spread flux method, using an original and nontoxic solvent, and growth setup design operative in air and at half the melting temperature of these compounds, can be optimally doped for high-power laser applications, without OH^- groups dissolution, without Yb^{3+} ions reduction into Yb^{2+} ones and with broader absorption and emission lines in the NIR spectral range. Such a broadness, as well as anti-Stokes emission spectra, were discussed within the scope of an exhaustive chemical analysis of the samples by GDMS which established that this flux growth process has the ability to purify the lutetia crystals for Er, Tm, Nd, Dy and Fe impurities but contaminates them with Li and B atoms. It is found that up to an Y^{3+} substitution rate of 6 % this growth technique drastically hinders the formation kinetics of Yb^{3+} pairs that would lead to cooperative emission around 500 nm detrimental to the fluorescence quantum yield of the Yb^{3+} ions near infrared (NIR) emission. Yb^{3+} absorption and stimulated emission cross sections in cubic $Gd_{1.72}Yb_{0.28}O_3$ crystals at the zero phonon line were found to reach ~1.6 10^{-20} and 2.8 10^{-20} cm^2, respectively, and the experimental lifetime ~0.48 ms. The trend in laser slopes is consistent with fluorescence quantum yield and partly interpreted by means of GDMS trace element analysis.

Acknowledgments

The authors would like to thank the Aquitaine Region, the GIS "Advanced Materials in Aquitaine", the "pôle de compétitivité" photonics in Aquitaine "Route des Lasers" and the French "Agence Nationale de la Recherche" (decision n° ANR 2010 JCJC 0909 01), for supporting this work.

References

1. A. Yoshikawa and V. Chani, MRS Bulletin, 34 (2009) 266.
2. A. Fukabori, V. Chani, K. Kamada, F. Moretti and A. Yoshikawa, Cryst. Growth & Des., 11 (2011) 2404.
3. R. Peters, C. Kränkel, K. Petermann and G. Huber, J. Cryst. Growth, 310 (2008) 1934.
4. C. Baer, C. Kränkel, C. J. Saraceno, O. H. Heckl, M. Golling, R. Peters, K. Petermann, T. Südmeyer, G. Huber and U. Keller, Opt. Lett., 35 (13) (2010) 2302.
5. P. Veber, M. Velázquez, V. Jubera, S. Pechev. and O. Viraphong, Cryst. Eng. Comm. 13 (16) (2011) 5220.
6. B. Weichelt, K. Wentsch, A. Voss, M. Abdou Ahmed, Th. Graf, Laser Phys. Lett., (2012) 110–115.
7. C. McMillen, D. Thomson, T. Tritt and J. Kolis, Cryst. Growth & Des., 11 (10) (2011) 4386.
8. A. Fukabori, V. Chani, K. Kamada, A. Yoshikawa, J. Cryst. Growth, 352 (2012) 124.
9. "*Laser demonstration with highly doped Yb^{3+}-Gd_2O_3 and Yb^{3+}-Y_2O_3 crystals grown by an original flux method*", Frédéric Druon, Matias Velázquez, Philippe Veber, Sylvie Janicot, Oudomsack Viraphong, Gabriel Buşe, Marwan Abdou Ahmed, Thomas Graf, Daniel Rytz, Patrick Georges, Optics Letters, 38 (20) (2013) 4146-4149.
10. V. Peters, *Growth and spectroscopy of Ytterbium-doped sesquioxides*, PhD thesis, University of Hamburg, Germany, (2001).
11. S. Hraïech, *Monocristaux cubiques de sesquioxydes Ln_2O_3 (Ln=Y, Lu et Sc) et de fluorures CaF_2 dopés par l'ion terre rare laser Yb^{3+} : croissance, caractérisation structurale et spectroscopie*, PhD thesis, University Claude Bernard of Lyon 1, France, (2007).
12. G. Buse, M. Velázquez, Ph. Veber. V. Jubera, Y. Petit, S. Péchev, O. Viraphong, R. Decourt, A. Jaffres, P. Aschehoug, G. Aka, Proc. SPIE 8433, Laser Sources and Applications, 84331B (June 1, 2012).
13. F. Auzel, G. Baldacchini, L. Laversenne and G. Boulon, Opt. Mater., 24 (2003) 103.
14. L. Laversenne, Y. Guyot, C. Goutaudier, M.-Th. Cohen-Adad, G. Boulon, Opt. Mater., 16 (2001) 475.

15. F. Auzel, Ann. Télécom., 24 (5-6) (1969) 199.
16. S. A. Payne, L. L. Chase, K. L. Smith, W. L. Kway and W. F. Krupke, IEEE J. Quant. Elect., 28 (11) (1992) 2619.
17. G. Boulon, J. All. Comp. 451 (2008) 1.
18. C. K. Jørgensen, J. Phys. C7, S n° 12, t 48 (1987) 447.
19. M. J. Weber, Phys. Rev., 171 (1968) 283.
20. L. A. Riseberg and H. W. Moos, Phys. Rev., 174 (1968) 429.
21. J. M. F. Van Dijk and M. F. H. Schuurmans, J. Chem. Phys., 78 (9) (1983) 5317.
22. E. Nakazawa and S. Shionoya, "Cooperative luminescence in $YbPO_4$", Phys. Rev. Lett., 25 (25), (1970) 1710–1712.
23. F. Auzel, Proc. IEEE 61 (1973) 758.
24. F. Auzel, C. R. Acad. Sci. Paris, 262 (1966) 1016–1019.
25. F. Auzel, C. R. Acad. Sci. Paris, 263 (1966) 819–821.
26. B. Schaudel, P. Goldner, M. Prassas and F. Auzel, "*Cooperative luminescence as a probe of clustering in Yb^{3+} doped glasses*", J. Alloys Comp., 300 (2000) 443–449.
27. P. Goldner, B. Schaudel and M. Prassas, "*Dependence of cooperative luminescence intensity on Yb^{3+} spatial distribution in crystals and glasses*", Phys. Rev. B, 65 (5), (2002) 054103.
28. R. Buisson and J.-C. Vial, J. Physique-LETTRES, 42, (1981) L115-L118.
29. F. Rosenberger, H. G. Riveros, J. Chem. Phys., 60 (2) (1974) 668-673.

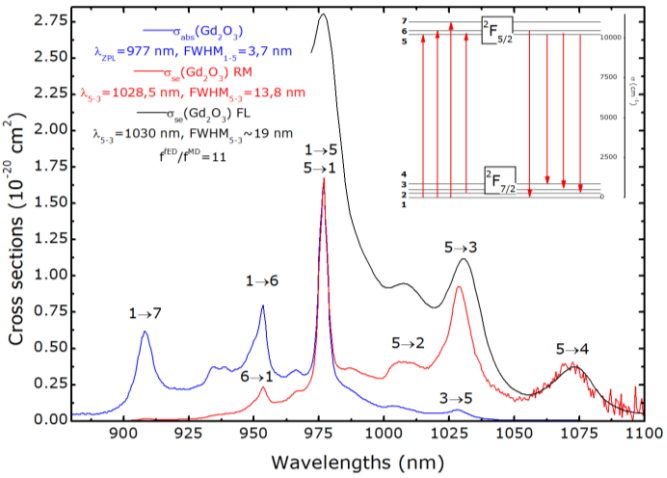

Fig. 1. Absorption and stimulated emission cross-sections of a cubic $Gd_{1.72}Yb_{0.28}O_3$ crystal grown by the flux method. The excitation wavelength of the Fuchtbauer-Ladenburg (FL)-calibrated spectrum was 932 nm. RM stands for reciprocity method.

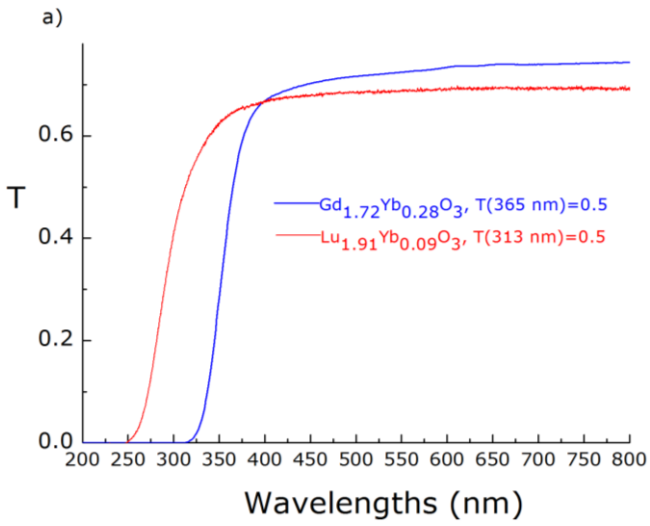

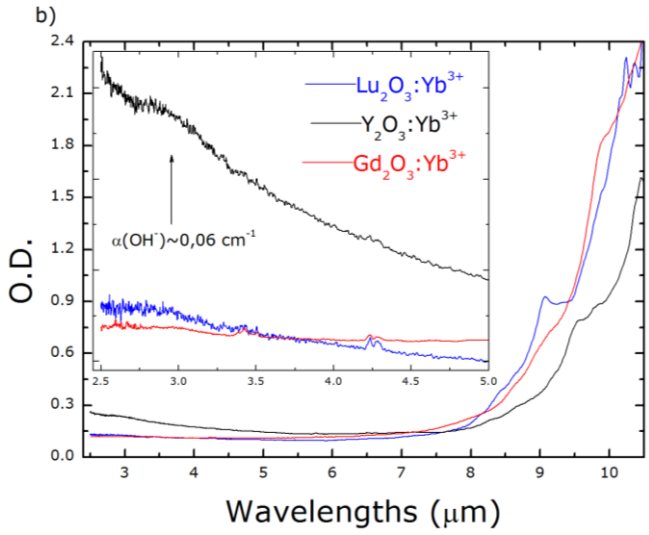

Fig. 2. (a) Visible and near UV transmission, uncorrected for reflection losses, of the Yb^{3+}-doped cubic gadolinia (t=3.02 mm) and lutetia (t=1.11 mm) crystals grown by the flux method. (b) FTIR spectra of Yb^{3+}-doped cubic gadolinia, yttria and lutetia crystals.

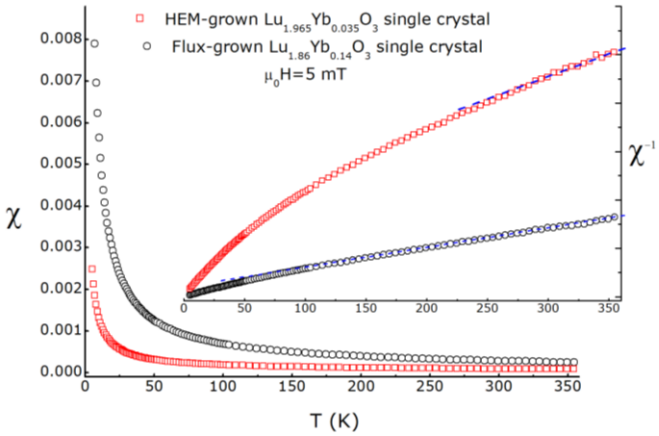

Fig. 3. MKSA magnetic susceptibility and inverse magnetic susceptibility of a $Lu_{1.86}Yb_{0.14}O_3$ flux-grown crystal and an HEM-grown $Lu_{1.965}Yb_{0.035}O_3$ crystal. The blue dashed line is a guide to visualize the Curie-Weiss behavior or what could potentially be interpreted in terms of such behavior.

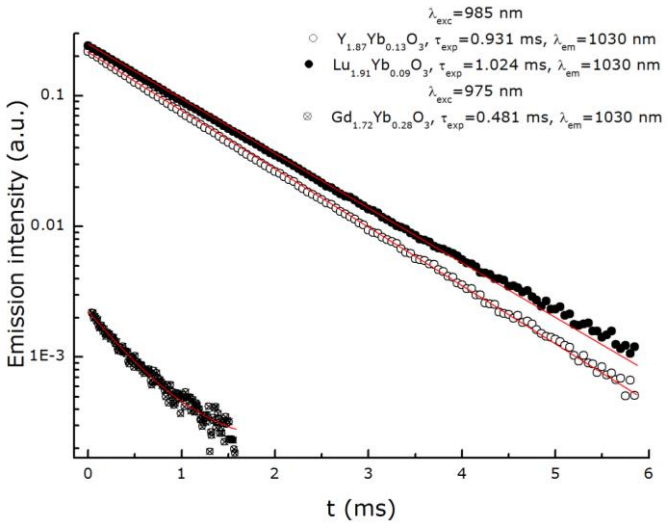

Fig. 4. Yb^{3+} ions fluorescence decays in gadolinia, yttria and lutetia single crystals grown by the flux method, at λ_{em}=1030 nm under λ_{exc}=985 nm for the two latters and λ_{exc}=975 nm for the former.

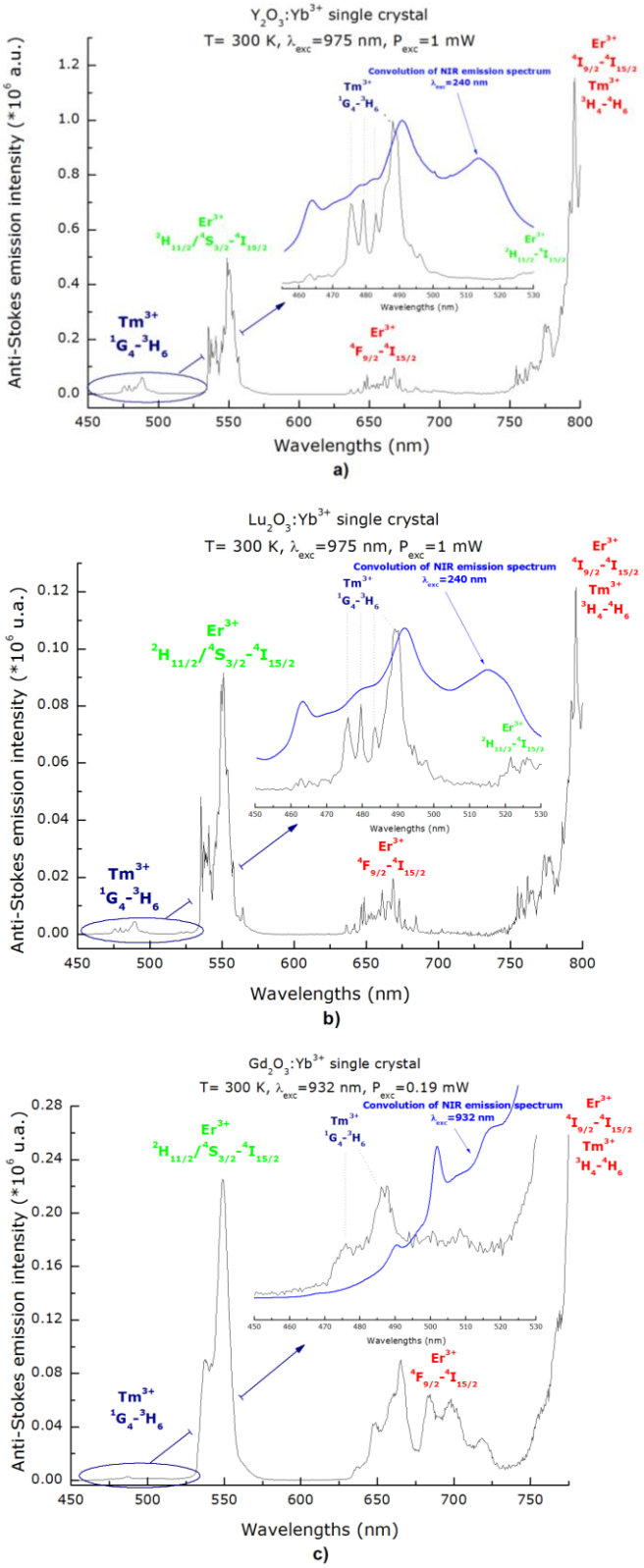

Fig. 5. Room temperature anti-Stokes emission spectra of Y_2O_3:Yb^{3+} (a) Lu_2O_3:Yb^{3+} (b) and Gd_2O_3:Yb^{3+} (c) single crystals obtained under excitation at 975 nm for the two former and at 932 nm for the latter.

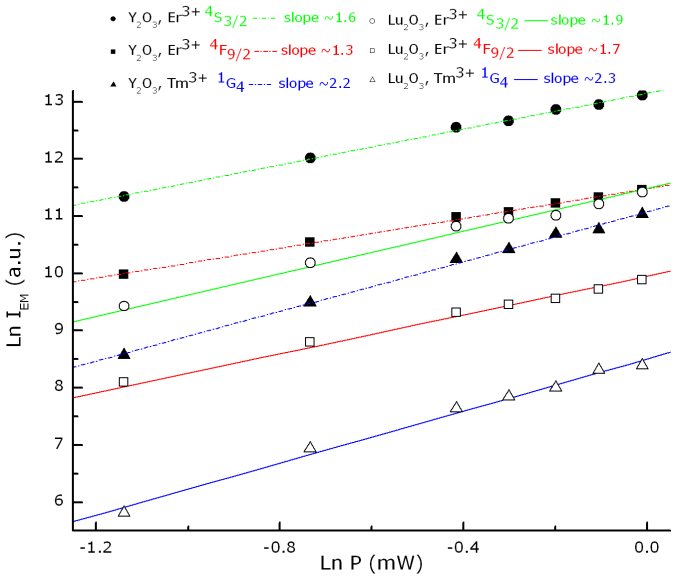

Fig. 6. Ln-Ln plots of the anti-Stokes emission intensity dependency on excitation power in $Y_2O_3:Yb^{3+}$ and $Lu_2O_3:Yb^{3+}$ single crystals, for excitation powers lower than 1 mW.

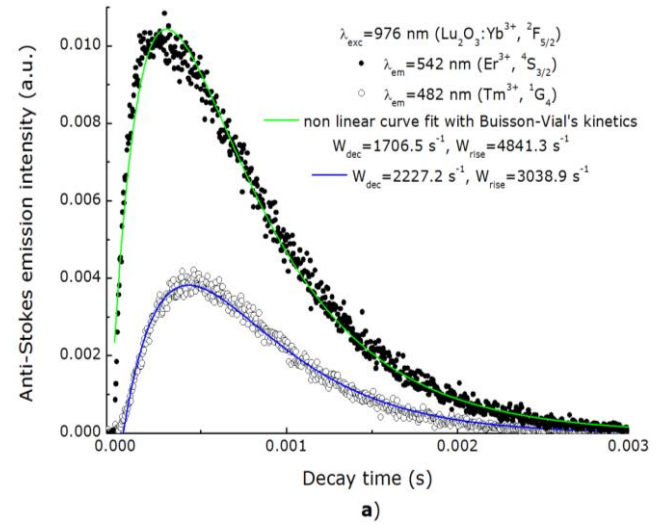

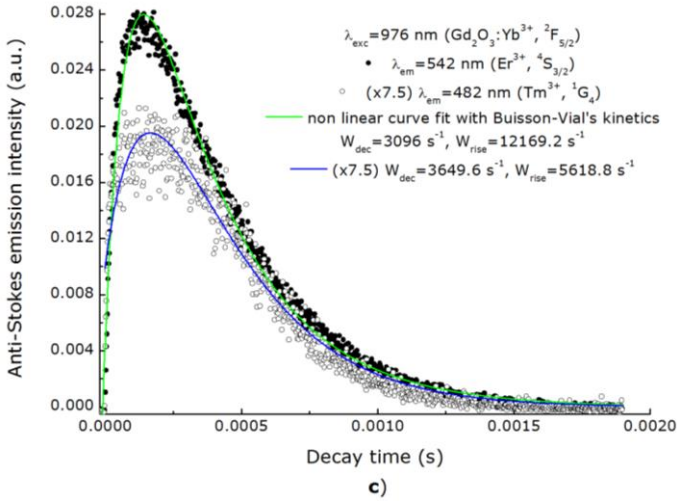

Fig. 7. Room temperature anti-Stokes fluorescence transients from levels $^4S_{3/2}$ of Er^{3+}- and $^1G_4$ of Tm^{3+}-contaminations in Yb^{3+}-doped Lu_2O_3 (a), Y_2O_3 (b) and Gd_2O_3 (c) single crystals, obtained under excitation at 976 nm.

Table 1
Maximum impurity concentration expected in the growth loads and impurity concentrations found in the flux grown $Lu_{1.91}Yb_{0.09}O_3$ and $Gd_{1.72}Yb_{0.28}O_3$ crystals.

Initial maximum impurity concentration	$Y_{1.87}Yb_{0.13}O_3$ (cm^{-3})	$Gd_{1.72}Yb_{0.28}O_3$ (cm^{-3})	$Lu_{1.91}Yb_{0.09}O_3$ (cm^{-3})
Er	$(3–5)\cdot10^{15}$	10^{15}	$2\cdot10^{16}$
Tm	$(0.4–2)\cdot10^{16}$	$<10^{15}$	$8\cdot10^{16}$
Nd	$8\cdot10^{15}$	$3\cdot10^{15}$	10^{15}
Dy	$3\cdot10^{15}$	$6\cdot10^{14}$	$9\cdot10^{15}$
Fe	$(0.2–2)\cdot10^{17}$	$5\cdot10^{16}$	10^{18}
Li	$<10^{14}$	$<10^{14}$	$<10^{14}$
B	$<10^{14}$	$<10^{14}$	$<10^{14}$

Impurity concentrations found in the $Lu_{1.91}Yb_{0.09}O_3$ crystal.
$[Er] = 3.7\cdot10^{15}$ cm^{-3}, $[Tm] = 1.1\cdot10^{16}$ cm^{-3}, $[Nd] = 3.9\cdot10^{14}$ cm^{-3}, $[Dy] = 10^{15}$ cm^{-3}.
$[Fe] = 10^{16}$ cm^{-3}, $[Li] = 2.9\cdot10^{17}$ cm^{-3}, $[B] = 3.2\cdot10^{17}$ cm^{-3}.
Na, Mg, Si, P, K, Zn, As, Y, Zr, Sb, Ce, Gd $\sim 10^{16}$ cm^{-3}.
Al, Ti, Cu, Ba, Tb $\sim 10^{15}$ cm^{-3}.
La $\sim 10^{14}$ cm^{-3}.
Impurity concentrations found in the $Gd_{1.72}Yb_{0.28}O_3$ crystal.
$[Er] = 2.4\cdot10^{16}$ cm^{-3}, $[Tm] = 4.5\cdot10^{16}$ cm^{-3}, $[Nd] = 3.6\cdot10^{16}$ cm^{-3}, $[Dy] = 2.5\cdot10^{17}$ cm^{-3}.
$[Fe] = 1.7\cdot10^{17}$ cm^{-3}, $[Li] = 1.8\cdot10^{19}$ cm^{-3}, $[B] = 3.9\cdot10^{18}$ cm^{-3}, $[Y] = 1.3\cdot10^{18}$ cm^{-3}, $[Ce] = 9\cdot10^{18}$ cm^{-3}.
Na, Al, Si, Ca, Zr, Tb $\sim 10^{17}$ cm^{-3}.
Mg, K, Ti, Cu, Zn, Sb, La, Eu, Sm $\sim 10^{16}$ cm^{-3}.
P, Ba, Pr $\sim 10^{15}$ cm^{-3}.